Autonomous observer of hydrogen storage to enhance a model predictive control structure for building microgrids

Daniela Yassuda Yamashita [a, b, *], Ionel Vechiu [a], Jean Paul Gaubert [b], Samuel Jupin [a]

[a] ESTIA Institute of Technology, Bidart, France
[b] Laboratoire d'Informatique et d'Automatique pour les Systèmes (LIAS), Université de Poitiers, Poitiers, France

ABSTRACT

Hydrogen energy storage has emerged as a promising technology to improve the integration of renewable energy sources in building microgrids. However, inaccuracies in the modelling of fuel cells and electrolysers reduce the performance of building microgrids' energy management system. To improve the flexibility of building microgrids, this paper proposes to associate a two-level hierarchical model predictive controller empowered with an Autonomous Observer of Hydrogen Storage (AOHS). This novel observer evaluates the hydrogen production and consumption rates, storing little past data and needing no tuning of the parameters. Relying only on instantaneous data measurement, the algorithm can estimate the tank's level of hydrogen with an average relative error inferior to 2 %, even under measurement noise. A case-study based on a building microgrid currently under construction serves as the basis for all simulations. The performance of the AOHS is evaluated by comparing the self-consumption rates of the case-study when governed by two-level energy management system: one level using a fixed parameters model and the other one equipped with the proposed AOHS algorithm. Results show that the microgrid associated to the AOHS has better self-consumption compared to the microgrid with fixed parameters, as well as a better robustness regarding the measurement noise and modelling error. Furthermore, this algorithm demonstrates a planning function as it facilitates the energy planning from the aggregator's point of view and the external grid management.

1. Introduction

Even though energy is essential for society, the energy sector is built on an unsustainable system that meets about 70 % of the primary energy demand with fossil fuel and nuclear power plants [1]. To foster the decarbonisation of the electricity systems, the fast energy transitioning scenario aims to integrate more than 5 thousand TWh of Photovoltaic (PV) panels into the grid by 2050 [1]. In this context, building microgrids, such as the ones described in [2–5], have emerged as a promising grid topology to enable the massive installation of renewable energy sources directly in the distribution sector.

To avoid radical changes in the electricity system when incorporating building microgrids into the current power grid, the simplification of the role of market operators is paramount. This simplification is performed by introducing the concept of self-consumption of PV electricity [6]. This grid regulation aims to minimise the building's microgrid daily power imbalance, allowing grid operators to supply the energy demand as efficiently as possible [7].

To attain high levels of self-consumption, energy storage systems (ESSs) are key elements to shift the building local energy surplus toward periods of energy deficit [8]. Particularly, due to the seasonality throughout the year, the combination of short- and long-term ESSs is increasingly envisaged for building microgrid implementation [9]. In recent years, hydrogen-based storage systems have become important seasonal ESSs, thanks to their high energy capacity (300–1200 Wh/kg) and their nearly zero self-discharging rates [10–12].

To take full advantages of hybrid ESSs while maximising PV self-consumption, it is necessary to design a proper building energy management system (EMS) [4]. Nonetheless, buildings are not homogeneous and require solutions tailored to their specific conditions. Therefore, this paper aims to propose a flexible solution to adapt EMSs to any hydrogen-based building microgrid automatically and independently of the electrical equipment size.

Among the existent EMS algorithms [13,14], model predictive control (MPC) has proved its robustness against environmental disturbances [15–17]. The capacity to consider prediction data and periodic optimisations over a sliding window are the main strengths of the MPC

Abbreviations

AOHS	Autonomous observer of hydrogen system
EMPC	Economic model predictive control
EMS	Energy management system
ESS	Energy storage system
HMPC	Hierarchical model predictive control
LoH	Level of hydrogen
MILP	Mixed-Integer Linear Programming
MPC	Model predictive control
PEM	Proton exchange membrane
PEME	Proton exchange membrane electrolyser
PEMFC	Proton exchange membrane fuel cell
PV	Photovoltaic panels
SoC	State of charge
TMPC	Tracking model predictive control

Variables

E_{grid}^{import}	Energy imported from the grid (Wh)
E_{grid}^{inject}	Energy injected from the grid (Wh)
T_s	Discrete sampling time of MPC (h)
E_{cons}	Energy consumed by the building (Wh)
E_{pv}	Energy generated by photovoltaic panels (Wh)
SoC_{ref}	Battery state of charge reference (%)
LoH_{ref}	Level of hydrogen reference (%)
τ_{sc}	Self-consumption rate (%)
τ_c	Coverage rate (%)
P_{fc}	Fuel cell operating power (W)
P_{bat}	Battery operating power (W)
P_{els}	Electrolyser operating power (W)
P_i^{max}	Maximum operating power (W), $i = \{bat, els, fc\}$
δ_{els}	Integer variable indicating whether the electrolyser is operating
δ_{fc}	Integer variable indicating whether the fuel cell is operating
δ_{bat}^{ch}	Integer variable indicating whether the battery is charging
δ_{bat}^{dis}	Integer n variable indicating whether the battery is discharging
f_{bat}	Linear function to predict the energy stored in the battery pack
f_{H_2}	Linear function to predict the energy stored in hydrogen tank
θ_{els}	Coefficient linking the level of hydrogen and electrolyser power (% /W)
θ_{fc}	Coefficient linking the level of hydrogen and fuel cell power (% /W)
V_{tank}	Normalized tank volume (Nm^3)
ς_{els}	Hydrogen production coefficient (kWh/Nm^3)
ς_{fc}	Hydrogen consumption coefficient (Nm^3/kWh)
PEM	Set referring to fuel cell or electrolyser. $PEM = \{fc, els\}$
$\dot{n}_{H_2}^{PEM}$	Hydrogen flow throughout fuel cell or electrolyser (mol/s)
N_{cells}^{PEM}	Number of cells in fuel cell or electrolyser stack
F	Faraday constant (A s mol^{-1})
R	Ideal gas constant (m^3 Pa K^{-1} mol^{-1})
$\beta_{Faraday}^{PEM}$	Angular coefficient linking the current in electrolyser or fuel cell with the tank's pressure variation ($\Delta P_{tank,\,k}$) (Pa A^{-1})
$P_{tank,\,k}^{meas}$	Measure of the tank pressure at instant k (bar)
P_{tank}^{max}	Maximum pressure supported by the tank (bar)
i_{PEM}^{meas}	Current measurement in the electrolyser or fuel cell stacks (A)
v_{PEM}^{meas}	Voltage measurement in the electrolyser or fuel cell stacks (V)
A, B and C	Vertices of the linear hydrogen linear model
P_{PEM}^{zonei}	Power zones of electrolyser or fuel cell, where $i \in \{1,2,3\}$ (W)
α_{PEM}^{zonei}	Angular coefficient linking the current and power consumed by the electrolyser or fuel cell if it is in power zone $i \in \{1,2,3\}$ (A W^{-1})
M_k	Measure point at instant k
$G_{zone_i}{}^x$	X-coordinate of the median of the three-zone power lines
$\sigma_{PEM,\,k}$	Approximate angular coefficient linking the current and power consumed/generated by the electrolyser or fuel cell

structure, making it highly appreciated for industrial applications. However, the performance of the MPC structure strongly depends on the quality of the predictions and on the models used.

In the context of long-term power flow optimisation, as it occurs in energy management for building microgrids, MPC requires precise ESS models. However, in the literature, MPC architectures are usually composed of time-invariant parameters derived from the manufacturer's technical specifications, therefore holding inaccuracies concerning the real system [18]. To improve the model precision, a model can be devised from the linearisation of non-linear experimental curves [15] or by fitting sample measurements to a logarithmic equation [19]. Alternatively, advanced techniques to estimate the intrinsic parameters of proton exchange membrane (PEM) fuel cell and PEM electrolyser result in a precise estimation of the tank level-of-hydrogen. For instance, models based on the physical structure of the PEM fuel cell lead to an accurate model [20]. Similarly, Kalman filters and sliding mode observers [21] anticipate fuel cell model changes such as oxygen and hydrogen partial pressure and stack temperature. However, these models are too complex to be embedded in MPC prediction as it requires many parameters that are usually hard to measure. Furthermore, these methods are usually time-invariant which may be inaccurate for long-term operation, especially due to the ageing of components and unexpected changes in the operating environment.

Aiming to reduce the effects of both imprecision in model-based state estimation and stochasticity in the building microgrid power imbalance

without raising the complexity of the MPC algorithm, this paper proposes the association of a two-level hierarchical MPC structure with an Autonomous Observer of Hydrogen Storage (AOHS). The primary objective of the proposed EMS is to maximise the annual self-consumption rate by optimising the building microgrid power flow. The innovation of the proposed EMS resides in the use of the AOHS and its direct inclusion in the MPC algorithm. This way, no parameter needs to be tuned to set up the MPC framework. Thanks to online data processing embedded in the AOHS, the EMS is capable of identifying the hydrogen ESS model parameters even under noise measurements. Moreover, the proposed AOHS algorithm achieves a highly precise modelling performance without storing past measurements. Consequently, the identification of the hydrogen ESS model is implemented only using a few stored variables.

The remainder of this paper is organised as follows. Section 2 presents the context of the building microgrid and this paper's case-study. Section 3 describes the hierarchical MPC structure by highlighting its cost function and constraints. Section 4 details the hydrogen ESS autonomous observer. Section 5 compares the performance of an MPC architecture associated with the AOHS algorithm with a classical MPC architecture without an AOHS. Finally, Section 6 concludes this paper.

2. The context of the building microgrid

The building microgrid selected as a case study is the future grid-

connected microgrid that will be installed in the existing building of ESTIA Institute of Technology in Bidart, France. This medium-sized public building will be equipped with PV solar panels, Li-ion batteries and a hydrogen energy storage system with technical specifications presented in Table 1. The resulting microgrid is represented in Fig. 4, where the different elements and their connections are displayed, as well as the control structure, discussed further in Section 3.

Since the objective of the building microgrid is to supply as much of its energy demand as possible with renewable energy, the PV panels will be controlled via the maximum power point tracking algorithm [22]. The PV power generation was modelled using real profiles of solar irradiation and temperature in Bidart [23], resulting in the annual power generation shown in Fig. 1. On the other hand, the building energy consumption – shown in Fig. 2 – follows the energy demand profile of the ESTIA building, in which weekends and holidays were considered for conceiving the dataset. It is worth noting that the building demand is about 25 % more elevated during the winter than in summer days due to heating devices.

Due to low PV energy capacity, the energy exchange between the grid and the building microgrid is moderated by a community aggregator [24]. In this configuration, prosumers send their day-ahead forecast load consumption and energy injection to the aggregator. After that, the aggregator buys (or sells) electricity from the market operator at wholesale market prices and sells to (or purchases from) prosumers in the microgrid community at retail market prices. Consequently, the building EMS must provide a one-hour resolution day-ahead grid energy exchange plan to the community aggregators.

One important restriction imposed by French grid regulations is the limitation concerning the annual energy injected into the grid [25]. The current grid code allows building microgrids to inject only the renewable energy generated locally and restricts building microgrids from discharging their ESSs to inject into the grid. Moreover, the building microgrid must be well-sized to minimise the annual PV energy generation injected into the public grid.

Therefore, to reduce the energy injection and maximise the annual PV self-consumption rate, the building microgrid has to optimise its power flow by assigning the right setting points for its hybrid ESS. Particularly, to handle the seasonality throughout the year, the building microgrid under study will rely on a hydrogen energy storage which can reserve energy long-term, which enables shifting the summer energy surplus to the periods of energy deficit during the winter. In particular, the building microgrid is equipped with PEM technology for electrolysis and fuel cells. This kind of technology can be coupled with RESs, thanks to its faster response time and lower degradation rate when subjected to an intermittent power rate, compared to other technologies [26].

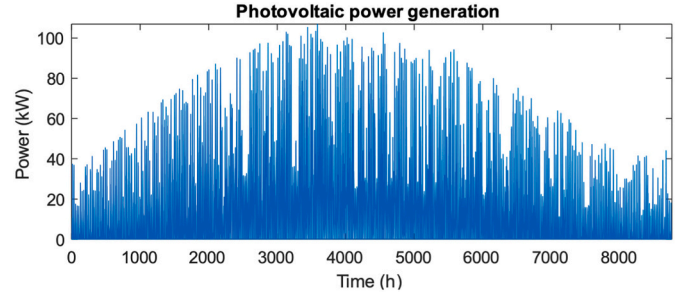The power-to-power hydrogen ESS includes three main parts: a

Fig. 1. Photovoltaic power generation during an entire year, from January to December.

hydrogen producer device (fuel cell), a hydrogen consumer device (electrolyser), and the hydrogen reservoir (tank), as shown in Fig. 4. The electrolysis reaction happening in the PEM electrolyser cells converts water and electricity into heat, oxygen and hydrogen gases, as described in Eqs. (1)–(3) [27]. As shown in Fig. 3a, the electrons pass through the electrical circuit attached to the electrolyser, while protons pass through the membrane dividing the anode and cathode. Subsequently, the protons arriving through the PEME membrane at the cathode combine with the electrons arriving through the ancillary electrical circuit, generating hydrogen in the gaseous form.

Complete electrolysis chemical reaction :

$$H_2O \rightarrow H_2 + \frac{1}{2}O_2 \qquad (1)$$

$$Anode : H_2O \rightarrow 2H^+ + \frac{1}{2}O_2 + 2e^- \qquad (2)$$

$$Cathode : 2H^+ + 2e^- \rightarrow H_2 \qquad (3)$$

The hydrogen produced in the cathode side of the PEM electrolyser is pushed into the hydrogen tank by using a hydrogen compressor [28]. The compressor adapts the difference of pressure between the PEME cathode and the hydrogen reservoir pressure, enabling the hydrogen to flow inside the tank. The stored hydrogen can be used later to generate electric power according to the building needs by regulating the operating pointing of PEM fuel cells and the outlet hydrogen flow.

On the other hand, the chemical energy of the combustion of hydrogen with oxygen happening in the PEM fuel cells, produces water, electricity and heat, as specified in Eqs. (4)–(6) [27]. As illustrated in Fig. 3b, the electro-oxidation of the hydrogen happens in the anode side, while the electro-reduction of oxygen occurs in the cathode side. The regulation of the outlet hydrogen throughput is assured by setting up the position of a mechanical valve located in between the tank and the anode of PEM fuel cell, whereas the operating point of the PEMFC is assured by controlling its DC-DC power converter. One important remark to assure high PEM fuel cell electrochemical efficiency is that the PEM fuel cell hydrogen utilisation rate must be regulated to make the PEMFC consume all the hydrogen flowing throughout the cells. In this way, all hydrogen crossing the PEMFC is used to generated power, avoiding resources being wasted.

Complete combustion chemical reaction :

$$H_2 + \frac{1}{2}O_2 \rightarrow H_2O \qquad (4)$$

$$Anode : H_2 \rightarrow 2H^+ + 2e^- \qquad (5)$$

$$Cathode : \frac{1}{2}O_2 + 2H^+ + 2e^- \rightarrow H_2O \qquad (6)$$

3. Hierarchical model predictive control structure

To adapt ESTIA's building microgrid into the electrical grid structure

Table 1
Investigated building microgrid electrical components.

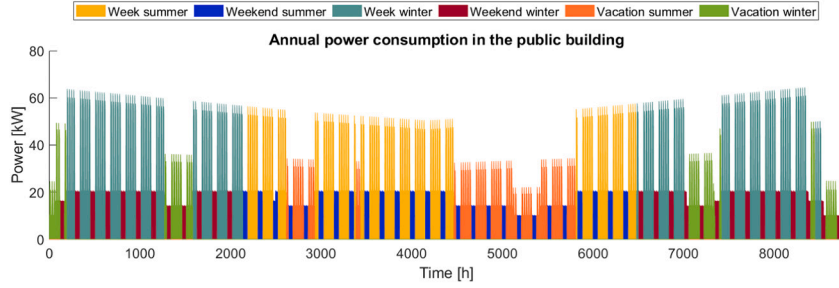| Equipment	Technical specification
Photovoltaic panels	Peak power at 1000 W/m^2: 107 kWc
	Annual energy generation: 131 MWh
Building load	Annual energy consumption: 242 MWh
Li-ion batteries	Nominal capacity: 167 Ah
	Nominal voltage: 720 V
	Nominal discharge current: 70A
	Maximum power rate: 60 kW
Hydrogen tank	Maximum pressure: 30 bars @ 80 °C
	Maximum hydrogen mass: 18 kg
	Normalized volume (V_{tank}): 224 Nm^3
PEM electrolyser	Nominal power: 25 kW
	Hydrogen production (ς_{els}): 4.18 kWh/Nm^3
	Maximum power rate: 30 kW
PEM fuel cells	Nominal power: 20 kW
	Hydrogen consumption (ς_{fc}): 0.63 Nm^3/kWh
	Maximum power rate: 48 kW
Compressor	Nominal power consumption (P_{comp}): 1 kW

Fig. 2. Annual building power consumption from January to December.
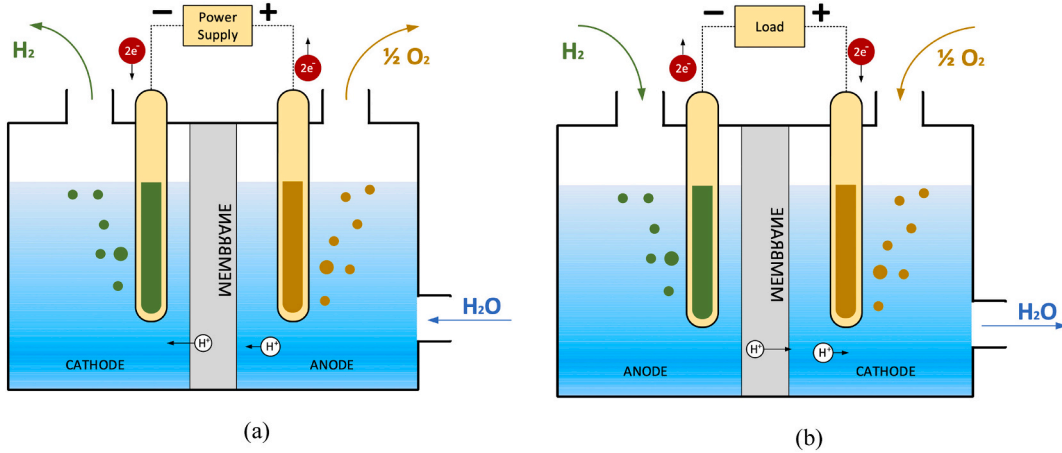

Fig. 3. Summary of chemical reaction in cathode and anode sides of (a) proton exchange membrane electrolysis cell and (b) proton exchange membrane fuel cells.

mentioned above, the two-level hierarchical MPC shown in Fig. 4 was designed. The proposed hierarchical EMS is composed of four individual control blocks, namely upper MPC, lower MPC, AOHS, and the community aggregator. They have different timescales and different roles in the general control structure. To assure the proper microgrid operation, they communicate with each other, by receiving information or transferring orders from one another. Therefore, the physical implementation of the algorithms is to be performed with different machines or different cores of the same real-time computer for each control element.

The community aggregator communicates with the external grid, buys or sells electricity, and receives the day-ahead planification of the
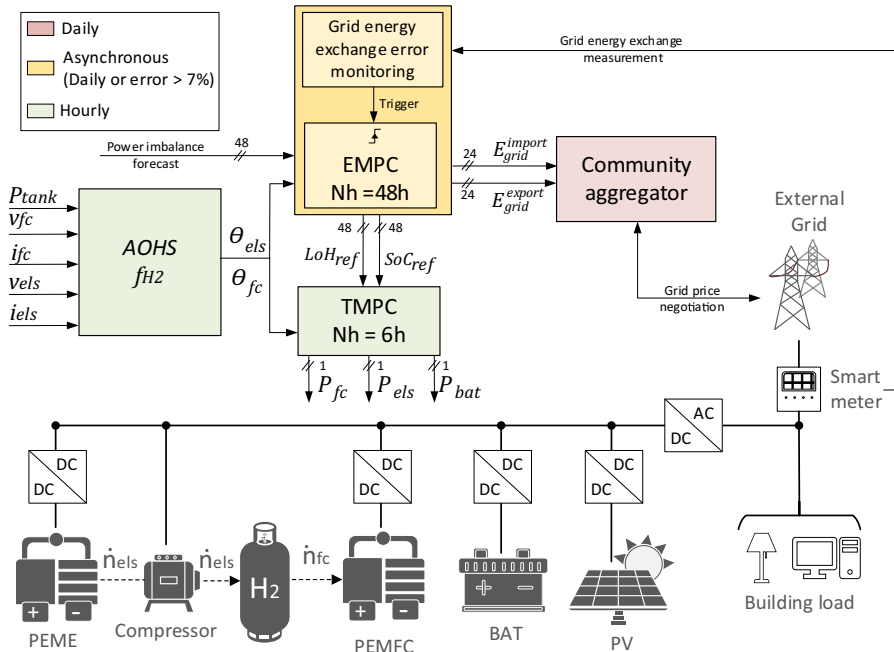

Fig. 4. Energy management system to optimise the power flow of a building microgrid.

building microgrid. The upper EMPC optimises the flow of energy, giving references to the lower MPC, in charge of managing the power flow. The AOHS measures the current behaviour of the hydrogen storage system and communicates dynamic parameters to both MPC algorithms.

Taking into account the stochasticity in the net power imbalance forecast ($E_{pv} - E_{cons}$), the upper MPC – named Economic MPC (EMPC) – determines the grid energy planning ($E_{grid,k}^{import}$ and $E_{grid,k}^{inject}$) for each discrete period k, where one period is an hour long ($T_s = 1$ h), the batteries state of charge ($SoC_{ref,k}$), and the tank level of hydrogen ($LoH_{ref,k}$). The objective of the EMPC is to minimise both the day-ahead energy imported ($E_{grid,k}^{import}$) and the energy injected into the grid ($E_{grid,k}^{inject}$). This is guaranteed through the optimisation of the cost function expressed in Eq. (7), solved using Mixed-Integer Linear Programming of the CPLEX.

$$min_{\theta} \sum_{k=1}^{48} E_{grid,k}^{import} + E_{grid,k}^{inject} \tag{7}$$

where $\theta = \left\{ SoC_{ref}, LoH_{ref}, E_{grid}^{import}, E_{grid}^{inject} \right\}$

The optimisation of Eq. (7) is implemented every day, at midnight or whenever the error between the planned energy exchange and the real imported and injected energy is higher than 7 %. This mechanism aims to reduce the number of unnecessary optimisations of the EMPC cost function.

Notably, the EMPC sends references for the battery state-of-charge (SoC) and the level of hydrogen (LoH) of the tank to the lower MPC, whereas the first 24 h of the grid energy planning (E_{grid}^{import} and $E_{grid}^{injected}$) are sent to the community aggregator. A horizon of 48 h was chosen to better estimate the SoC and the LoH at the end of the day. A prediction horizon twice longer than the daily optimisation prevents the controller from fully discharging its ESS unnecessarily, therefore keeping the optimality not only for the current day but also for the next one.

Meanwhile, the lower MPC aims to fulfil the grid exchange plan sent to the community aggregator by running the hybrid ESS at adequate power set points. Therefore, every hour it implements a tracking MPC (TMPC) to minimise the quadratic errors between the LoH and SoC references transmitted by the EMPC, as expressed in the cost function defined in Eq. (8). Its optimisation horizon is eight times shorter than the one of the upper MPC, so as to reduce the need for high computation resources. In this equation, each quadratic error is normalized regarding its respective maximum values and weighted to give more importance to instantaneous references than to farther references in the TMPC horizon. Consequently, TMPC will determine the power references for fuel cells (P_{fc}), electrolysers (P_{els}) and batteries (P_{bat}) that follow as much as possible the references of the upper MPC considering the updated ESS states.

$$min_{P_{fc},P_{els},P_{bat}} \sum_{k=1}^{6} \left(\frac{N_h^{TMPC} - k - 1}{SoC_{max}} \right)^2 \left(SoC_{ref,k} - \widehat{SoC_k} \right)^2$$
$$+ \left(\frac{N_h^{TMPC} - k - 1}{LoH_{max}} \right)^2 \left(LoH_{ref,k} - \widehat{LoH_k} \right)^2 \tag{8}$$

One of the most important goals of the hierarchical MPC is to keep the energy balance between load (E_{cons}) and generation (E_{pv}) by considering the equality constraint (9). In this equation, the power consumed by the hydrogen compressor (P_{comp}) to push the hydrogen into the tank is considered whenever the electrolyser is operating ($\delta_{els} = 1$). Furthermore, the hierarchical MPC optimisation is constrained to maintain the safe operation of each ESS by limiting their power rate according to its maximum and minimum values, as expressed in Eqs. (10) for the hydrogen storage and (11) for batteries. Notably, δ_{els}, δ_{fc}, δ_{bat}^{ch} and δ_{bat}^{dis} are integer variables that are worth one when the ESS is active; and zero, otherwise. To avoid charging and discharging batteries and prevent the controller from filling in and filling out the hydrogen tank simultaneously, the inequality constraints in Eq. (12) must be embedded into the two-level MPC.

$$E_{pv,k} - E_{cons,k} + T_s \left(P_{bat,k} + P_{els,k} + P_{fc,k} + P_{comp} \bullet \delta_{els,k} \right) + E_{grid,k}^{import} + E_{grid,k}^{injected} = 0 \tag{9}$$

$$-P_{els,k}^{max} \bullet \delta_{els,k} \leq P_{els,k} \leq 0;$$
$$0 \leq P_{fc,k} \leq P_{fc,k}^{max} \bullet \delta_{fc,k} \tag{10}$$

$$P_{bat,k}^{min} \bullet \delta_{bat,k}^{ch} \leq P_{bat,k}^{ch} \leq 0;$$
$$0 \leq P_{bat,k}^{dis} \leq P_{bat,k}^{max} \bullet \delta_{bat,k}^{dis} \tag{11}$$

$$0 \leq \delta_{els,k} + \delta_{fc,k} \leq 1;$$
$$0 \leq \delta_{bat,k}^{ch} + \delta_{bat,k}^{dis} \leq 1 \tag{12}$$

The hierarchical MPC also considers the grid code for small prosumers in France [29] by limiting the charging of ESSs with the internal power surplus ($P_{surplus}$) and constraining their discharging to only supply the building internal power deficit ($P_{deficit}$), as defined in Eqs. (13) and (14), respectively.

$$- \left| max \left(P_{bat}^{min} - P_{els,k}^{max}, P_{surplus} \right) \right| \leq P_{bat,k}^{ch} + P_{els,k} \leq 0 \tag{13}$$

$$0 \leq P_{bat,k}^{dis} + P_{fc,k} \leq \left| min \left(P_{bat}^{max} + P_{fc,k}^{max}, P_{deficit} \right) \right| \tag{14}$$

The hierarchical MPC structure decides to use the batteries or the hydrogen storage according to their round-trip energy efficiency, which are embedded into the MPC internal models through the inequality constraints defined in Eqs. (15) and (16). In these two equations, the values of SoC and LoH for the next period (SoC_{k+1} and LoH_{k+1}) are computed via the linear functions f_{bat} and f_{H2} that are calculated through autonomous observers.

In the case of batteries, an iterative algorithm that is further detailed in [30] determines the parameters of f_{bat}. On the other hand, the parameters of f_{H2} are updated daily by the AOHS algorithm detailed in the next section. The AOHS was briefly introduced in the authors' previous work [31] to explain the context of another study focusing on a technical-economic analysis of installation of hybrid ESS in building microgrids. In this paper, the AOHS is mathematically detailed, and its operation performance is analysed in depth. Additionally, contrary to the work presented in [31], in this paper, the AOHS robustness against measurement noise is assessed to verify its impact on the annual self-consumption rate.

$$SoC_{min} \leq SoC_{k+1} = SoC_k + f_{bat} \left(P_{bat,k}^{ch}, P_{bat,k}^{dis} \right) \leq SoC_{max} \tag{15}$$

$$LoH_{min} \leq LoH_{k+1} = LoH_k + f_{H2} \left(P_{els,k}, P_{fc,k} \right) \leq LoH_{max} \tag{16}$$

4. Algorithm of the AOHS

As shown in Fig. 4, in a closed loop with the hierarchical MPC structure and the hydrogen storage, the AOHS aims to continuously improve the precision of the LoH estimation. The proposed AOHS updates the parameters θ_{els} and θ_{fc} composing f_{H2} defined in Eq. (17). This operation is performed with the same sample time as the smallest controller's discretisation time ($T_s = 1$ h) and relies solely on local measurements. The θ_{els} and θ_{fc} parameters are determined either through physical values provided by the manufacturers ($\varsigma_{els}, \varsigma_{fc}$ and V_{tank} defined in Table 1) or through the process implemented by the AOHS.

$$f_{H2} \left(P_{els,k}, P_{fc,k} \right) = \underbrace{\frac{T_s}{\varsigma_{els} \cdot V_{tank} \cdot 1000}}_{\theta_{els,k}} P_{els,k} - \underbrace{\frac{\varsigma_{fc} \cdot T_s}{V_{tank} \cdot 1000}}_{\theta_{fc,k}} P_{fc,k} \tag{17}$$

The continuous identification of θ_{els} and θ_{fc} is based on two iterative correlation processes and on a step of model polishing. Each of these operations will be detailed in the next subsections.

4.1. Step 1: correlation between current and pressure variation

The relationship between the current and the tank pressure is inferred from the combination of Faraday's law of electrolysis with the ideal gas law. Defined by Eq. (18), Faraday's law of electrolysis links the current in the PEM stacks (i_{PEM} in A) to the hydrogen flowing ($\dot{n}_{H_2}^{PEM}$ in mol/s) [32]. In this equation, N_{cells}^{PEM} is the number of cells in the PEME or the PEMFC, and F is the Faraday constant in C/mol. Notably, the notation *PEM* refers to the set $PEM = \{fc, els\}$, referring to PEMFC or PEME, respectively.

$$\dot{n}_{H_2}^{PEM} = \frac{N_{cell}^{PEM} \cdot i_{PEM}}{2 \cdot F} \tag{18}$$

Considering that the temperature variation in the hydrogen tank is much slower than the model update time (T_s), the number of moles stored in the tank (n_{H2}^{tank}) is proportional to the tank pressure (P_{tank}), following the ideal gas law defined by Eq. (19), where R is the ideal gas constant in $\frac{\text{m}^3 \bullet \text{Pa}}{\text{K} \bullet \text{mol}}$. By computing the derivative, the hydrogen flow ($\dot{n}_{H_2,k}^{PEM}$) can be estimated from the variation of tank pressure. As a result, Faraday's equation in Eq. (18) can be rewritten in function of the tank pressure, instead of the number of moles, as shown in Eq. (20).

$$\frac{n_{H_2,k}^{tank}}{P_{tank,k}} = \frac{V_{tank}}{R \cdot T_{tank}} \xrightarrow{\frac{d}{dt}} \dot{n}_{H_2}^{tank} = \frac{V_{tank}}{R \cdot T_{tank}} \cdot \frac{P_{tank,k} - P_{tank,k-1}}{T_s} \tag{19}$$

$$\Delta P_{tank,k} = \underbrace{\frac{R \cdot T_{tank}}{V_{tank}} \cdot \frac{N_{cells}^{PEM}}{2 \cdot F} \cdot T_s}_{\beta_{Faraday}^{PEM}} \cdot i_{PEM} \tag{20}$$

Instead of attributing static values to compute $\beta_{Faraday}^{PEM}$ in Eq. (20), the AOHS algorithm determines it automatically thanks to a dynamic update process. To identify $\beta_{Faraday,k}^{PEM}$, the pressure and current measurements are used. The sample measurement composed by the couple $M_k = (\Delta P_{tank,k}^{meas}, i_{PEM,k}^{meas})$ are used to calculate $\beta_{Faraday,k}^{meas,PEM}$, by using Eq. (21), where $PEM = \{els, fc\}$ refers to either electrolyser or fuel cells.

$$\beta_{Faraday,k}^{meas,PEM} = \frac{\Delta P_{tank,k}^{meas}}{i_{PEM,k}^{meas}}, \; if \; i_{PEM,k}^{meas} \neq 0 \tag{21}$$

With the instantaneous value of $\beta_{Faraday,k}^{meas, PEM}$, the estimated value of $\beta_{Faraday,k}^{PEM}$ is updated through a weighted average between its last estimation and the current measurement, as specified in Eq. (22). As shown in Fig. 5 and defined in Eqs. (23) and (24), the variable $\omega_{PEM,k}$ is a confidence weight that grows with the acquisition of new measurements and is linearly reduced by a constant variable τ_{PEM}^{decay}. The value of τ_{PEM}^{decay} should be tuned according to the desired model robustness against noise measurement. Higher values of τ_{PEM}^{decay} will lead the model to adapt to changes in the external environment more easily, but it will reduce the model's robustness. Notably, the static parameter $\Delta\omega_{PEM}$ – also known as the learning rate – is the variation of the confidence weight between two

Fig. 5. Temporal evolution of pressure-current confident weights.

consecutive iterations. Therefore, the weight $\omega_{PEM,k}$ increases as soon as a new measurement M_k is acquired, following Eq. (23). Subsequently, at each iteration ($T_s = 1$ h), all confidence weights are reduced according to a pace defined by Eq. (24). Fig. 5 shows that the weights $\omega_{PEM=\{els,fc\}}$ decrease when the PEMFC or PEME are not operating.

$$\beta_{Faraday,k+1}^{PEM} = \frac{\omega_{PEM,k} \cdot \beta_{Faraday,k}^{PEM} + \Delta\omega_{PEM} \cdot \beta_{Faraday,k}^{meas,PEM}}{\omega_{PEM,k} + \Delta\omega_{PEM}} \tag{22}$$

$$\omega_{PEM,k} = \omega_{PEM,k} + \Delta\omega_{PEM}, \; if \; i_{PEM,k} \neq 0 \tag{23}$$

$$\omega_{PEM,k} = \omega_{PEM,k} - \tau_{PEM}^{decay} \tag{24}$$

4.2. Step 2: correlation between current and power

The relation between the current and the power is non-linear. Consequently, representing the hydrogen flow through the tank's inlet and outlet as a single linear function, as suggested in most studies [15,18], may result in modelling inaccuracies. Considering this problem, a new intermediary linear model based on the intensity of power is proposed. This novel linear model divides the power references assigned to electrolysers (P_{els}) and fuel cells (P_{fc}) into three operating zones, which leads to the definition of three powers for each PEM technology, namely P_{PEM}^{zone1}, P_{PEM}^{zone2} and P_{PEM}^{zone3}. The objective is to enhance the model accuracy by linearising the non-linear power-current curve shown in Fig. 6 into three linear functions.

Without storing any past measurements, the identification of these three lines relies only on the present measurements of the currents (i_{fc} and i_{els}) and of the voltages (v_{fc} and v_{els}) of PEMFC and PEME, and on the coordinates of three points, namely A, B and C. These three points are the vertices of the intersection between the power zones and the linear model, as shown in Fig. 6a. Therefore, as summarised in Table 2, their y-coordinates are fixed and dependent on the maximum power rate supported by each PEM technology (P_{PEM}^{max}), whereas their x-coordinates are defined by angular coefficients of each of the three lines, i.e. α_{PEM}^{zone1}, α_{PEM}^{zone2} and α_{PEM}^{zone3}. Consequently, the linear model is determined by the AOHS through the identification of these three angular coefficients.

At the first iteration, the vertices A, B, and C are initialised so that the three vertices are aligned with the first non-null measure M_k, as shown in Fig. 6a. Therefore, if the first point $M_k = (i_{PEM,k}^{meas}, v_{PEM,k}^{meas})$, in which $i_{PEM,k}^{meas} \neq 0$, then the three angular coefficient are worth $\alpha_{els,k}^{zone1} = \alpha_{els,k}^{zone2} = \alpha_{els,k}^{zone3} = 1/v_{PEM,k}^{meas}$.

Subsequently, for the next iterations, the vertices are updated according to the location of the measurement M_k. If the point M_k belongs to a specific power zone, then one of the vertices limiting this power zone will be modified. For instance, if the M_k is in zone3, as shown in Fig. 6b or c, either the vertices B or C will be modified. The upper vertex (point C) will be updated, if M_k is nearer to the vertex C than vertex B, as shown in Fig. 6b. On the opposite case, the lower vertex (point B) will be modified if the point M_k is nearer to vertex B than vertex C, as illustrated in Fig. 6c.

To update the upper vertex C, the angular coefficient of the third zone, i.e. α_{PEM}^{zone3}, is calculated. Implemented through Eq. (25), this updating process corresponds to a weighted dynamic averaging operation of the last estimation of the angular coefficient of the line $\overline{BC}$ (i.e. α_{fc}^{zone3}) and the new measured $\alpha_{fc,meas}^{zone3}$. The variable $\alpha_{fc,meas}^{zone3}$ is the angular coefficient of the line $\overline{BM_k}$ that is calculated through Eq. (26), whereas $\omega_{fc,k}^{zone3}$ is the confidence weight of the estimation of α_{fc}^{zone3}. The term $\Delta\omega_{fc}$ – also called learning rate – indicates the importance of the new measurement regarding the current estimation of α_{fc}^{zone3}. Both ω_{fc}^{zone3} and $\Delta\omega_{fc}$ are initialised to a small value, typically in the order of 0.1. The weight ω_{fc}^{zone3} grows with the acquisition of measurements close to the vertex C, following Eq. (25). To deal with the ageing of the PEMFC and PEME, at each sampling time ($T_s = 1$ h), the confident weights linearly decrease according to the variable τ_{decay}, as defined in Eq. (28).
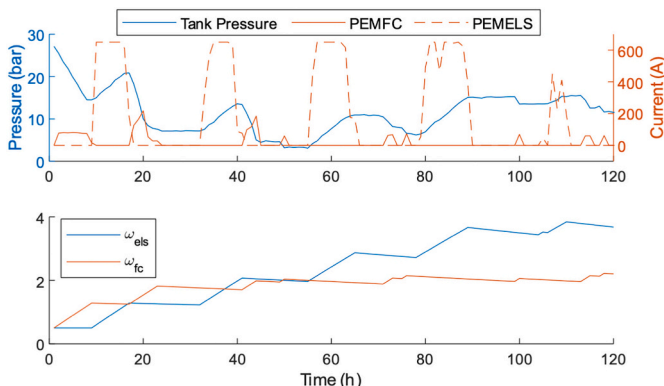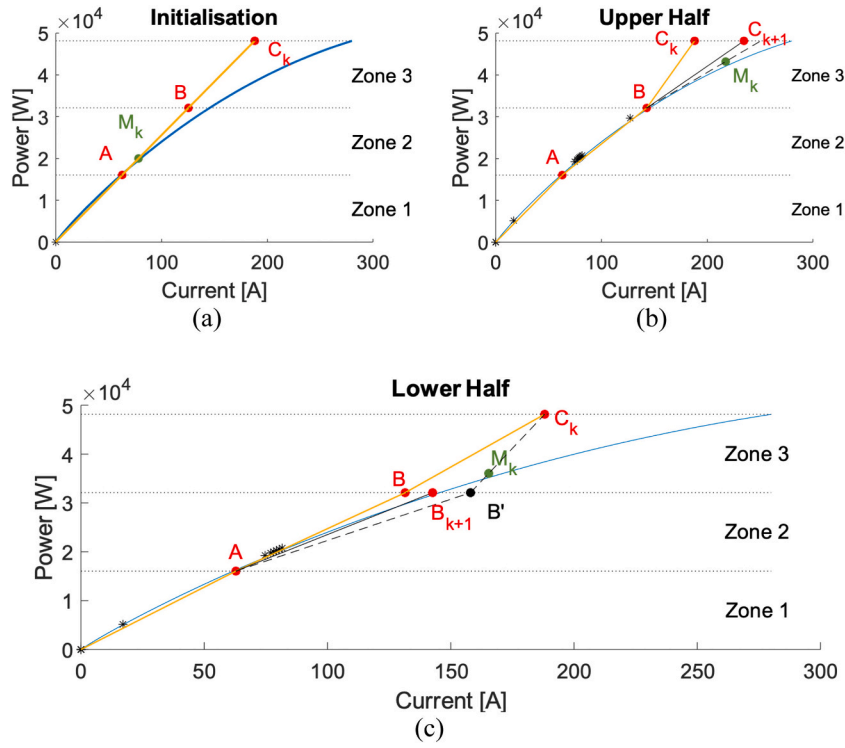
Fig. 6. Detail of the fuel cell RTMI. (a) Initialisation step. (b) Update step when the measurement point is near to the upper vertex. (c) Update step when the measurement point is near to the lower vertex.

Table 2
Coordinates of the vertices points A, B, and C.

Vertex point	x-Coordinate (current)	y-Coordinate (power)
A	$A_x^{PEM} = i_{PEM}^A$	$A_y^{PEM} = P_{PEM}^{max}/3$
B	$B_x^{PEM} = i_{PEM}^B$	$B_y^{PEM} = 2 \bullet P_{PEM}^{max}/3$
C	$C_x^{PEM} = i_{PEM}^C$	$C_y^{PEM} = P_{PEM}^{max}$

$$\alpha_{PEM,k+1}^{zone3} = \frac{\omega_{PEM,k}^{zone3} \cdot \alpha_{PEM,k}^{zone3} + \Delta\omega_{PEM} \cdot \alpha_{PEM,meas,k}^{zone3}}{\omega_{PEM,k}^{zone3} + \Delta\omega_{PEM}} \tag{25}$$

$$\alpha_{PEM,meas,k}^{zone3} = \frac{C_{y,k}^{PEM} - v_{PEM,k}^{meas}}{C_{x,k}^{PEM} - i_{PEM,k}^{meas}} \tag{26}$$

$$\omega_{PEM,k}^{zone3} = \omega_{PEM,k}^{zone3} + \Delta\omega_{PEM} \tag{27}$$

$$\omega_{PEM,k}^{zone3} = \omega_{PEM,k}^{zone3} - \tau_{decay} \tag{28}$$

In the opposite scenario, if the point M_k belongs to zone3 and is nearer to vertex B than vertex C, the x-coordinate of the vertex B is modified. Firstly, as shown in Fig. 6c, an intermediate point $B' = (B_x', B_y')$ is determined. This point B' corresponds to the intersection between $\overline{CM_k}$ and the line dividing zone 2 and zone 3. Subsequently, the point B is updated similarly to the upper vertex. Firstly, the angular coefficient of line $\overline{AB'}$, namely $\alpha_{fc, meas}^{zone2}$, is calculated through Eq. (29). Thereafter, the same update process of the upper vertex is applied to the lower vertex.

$$\alpha_{PEM,meas,k}^{zone2} = \frac{B_y' - A_{y,k}^{fc}}{B_x' - A_{x,k}^{fc}} \tag{29}$$

To better understand the second step of the algorithm, Fig. 7 shows the temporal evolution of the confident weights. As expected, the weights ω_{fc}^{zone1}, ω_{fc}^{zone1} and ω_{fc}^{zone1} grow when the PEME or PEMFC are operating and decrease when they are in an idle mode. After having identified the three angular coefficients (α_{PEM}^{zone1}, α_{PEM}^{zone2} and α_{PEM}^{zone3}), the
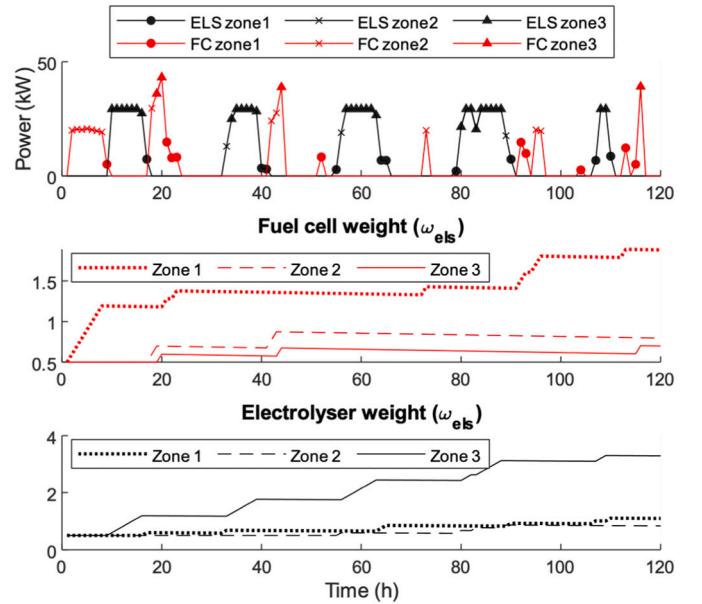

Fig. 7. Temporal evolution of power-current confident weights.

final step consists of determining a unique correlation parameter, namely σ_{PEM}, linking power to current, as expressed in Eq. (30). Instead of building a model with multiple variables – for instance, power at zone1, zone2 and zone3 – the idea is to facilitate the MILP optimisation process by including only two control variables, i.e. power references for PEMFC (P_{fc}) and PEME (P_{els}).

$$P_{PEM,k} = \sigma_{PEM,k} \cdot i_{PEM,k} \tag{30}$$

Therefore, from the values of the three angular coefficients, it is possible to determine $\sigma_{PEM, k}$ through the minimisation of the weighted

quadratic distance between the x-coordinate of the median of the three-zone power lines (G^x_{zone1}, G^x_{zone2} and G^x_{zone3}, as illustrated in Fig. 8) and the approximative linear model defined by Eq. (30). This approximation is assured by the minimisation of the cost function defined by Eq. (31).

$$\min_{\sigma_{PEM}} \sum_{i=1}^{3} \omega^{zone_i}_{PEM} \cdot \left(G^x_{zone_i} - \frac{(2 \cdot i - 1) \cdot P^{max}_{PEM}}{6 \cdot \sigma_{PEM}} \right)^2 \tag{31}$$

4.3. Step 3: approximation and definition of the linear model

The final step of the AOHS algorithm consists of building the final model by identifying the direct correlation between power (P_{els} and P_{fc}) and variation of the *LoH* ($\Delta LoH = f_{H2}(P_{els}, P_{fc})$). The real LoH can be estimated from the current tank pressure ($P^{meas}_{tank,\ k}$) and the maximum tank pressure (P^{max}_{tank}), as shown in Eq. (32). By combining this equation to the correlation between current and pressure variation determined in the first step ($\beta^{PEM}_{Faraday}$ of Eq. (22)) and the correlation between current and power (σ_{PEM} of Eq. (31)) calculated in the second step, it is possible to determine the direct link between power and variation of the LoH. Consequently, the function f_{H2} in Eq. (17) can be calculated using Eq. (33).

$$LoH_k = \frac{P^{meas}_{tank,k}}{P^{max}_{tank}} \tag{32}$$

$$f_{H2}\left(P_{fc,k}, P_{els,k}\right) = \underbrace{\frac{\beta^{fc}_{Faraday,k}}{\sigma_{fc,k} \cdot P^{max}_{tank}} P_{fc,k}}_{\theta_{fc}} + \underbrace{\frac{\beta^{els}_{Faraday,k}}{\sigma_{els,k} \cdot P^{max}_{tank}} P_{els,k}}_{\theta_{els}} \tag{33}$$

5. Case studies

To assess the performance of the MPC empowered with the AOHS algorithm, the building microgrid of sizing defined in Table 1 was simulated in MATLAB Simulink® using the PEMFC SimPower-Systems model and a PEME model validated through experimental data reported in [19]. The analysis of the proposed EMS is divided into two main parts. The first part is focused on the robustness of the proposed linear model against measurement noise. Meanwhile, the second part consists of a benchmark with the common linear model [18] defined by Eq. (17).

5.1. Precision and robustness against measurement noise

To verify the precision and the robustness of the proposed AOHS against measurement noise, the real voltage, current, and tank pressure measurements were disturbed by a normalized Gaussian noise of variance of 1 %, 5 %, and 10 % of their nominal values. To assess the error between the day-ahead LoH calculated by the EMPC and the real one, the TMPC in these scenarios was considered as a perfect router. Consequently, instead of optimising Eq. (8), it implements the control variables determined by the EMPC. Therefore, the effect of the TMPC is
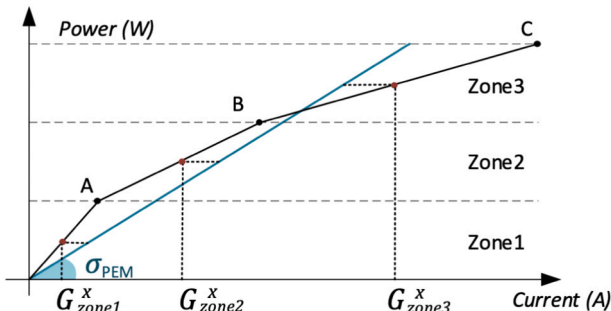

Fig. 8. Visualisation of the definition of the approximate model.

Table 3
Average precision of the level of hydrogen estimation according to the intensity of noise measurement.

LoH error	Noise measurement intensity				
	Theoretical	0 %	1 %	5 %	10 %
Average (p.p.)	0.57	0.77	0.75	1.2	0.68
Maximum (p.p.)	4.3	4.9	4.9	6.8	7.2

decoupled, highlighting the impact of errors in the estimated LoH.

After simulations of 50 days of operation of the PEMFC and PEME under these three measurement noise intensities, the temporal evolution of the current-voltage (σ_{fc} and σ_{els}) and current-pressure ($\beta^{els}_{Faraday}$ and $\beta^{fc}_{Faraday}$) correlation factors are shown in Fig. 10. It is noteworthy that in these simulations, $\Delta\omega_{PEM}$ and τ_{decay} were set up as 0.1 and 0.001, respectively. In addition, ω_{PEM}, ω^{zone1}_{PEM}, ω^{zone2}_{PEM} and ω^{zone3}_{PEM} were initialised as 0.5. Table 3 indicates that the AOHS can identify the current-power coefficients with an average error below 2 % regarding the theoretical model, whereas the pressure-current is determined with an average error inferior to 11 %. Notably, the theoretical model was obtained from the complete linear regression of the real PEME and PEMFC models.

Despite including a measurement noise with a variance of 10 %, the graphs in Fig. 10 highlight that the final estimated hydrogen storage parameters are close to the theoretical model, demonstrating that the proposed AOHS algorithm is robust, especially against voltage and current noise measurements. Nonetheless, since the algorithm is based on the variation of the pressure (Eq. (21)), the pressure measurement noise is amplified, harming the precision of pressure-current parameter identification ($\beta^{els}_{Faraday}$ and $\beta^{fc}_{Faraday}$), as shown in Fig. 9.

Besides its robustness, the precision of the proposed algorithm is comparable to the theoretical model. According to Table 3, the algorithm can assure almost the same average error under the three intensities of noise measurement, with an average difference below a 0.6 percentage point (p.p.) regarding the theoretical model. In particular, the AOHS demonstrated highly robust against noise measurement with variance inferior to 1 %, since the maximum and the average LoH errors were kept almost the same with 0 % and 1 % of noise variance.

Notwithstanding, as shown in Table 3, the maximum error in the estimation of the LoH when including noise measurements with a variance of 5 % and 10 % is higher than the theoretical model. As discussed previously and shown in Fig. 10, this is due to the inaccuracies in the estimation of the pressure-current correlation factors created by the computation of the pressure variation. Therefore, to keep the same precision as the theoretical model, a pressure measurement noise below 5 % must be guaranteed. This can be assured through the inclusion of moving average filters or using more precise pressure sensors.
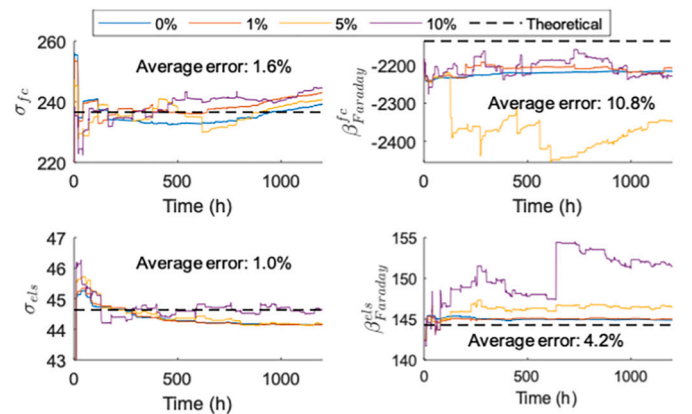

Fig. 9. Estimation of current-power (σ_{fc} and σ_{els}) and current-pressure ($\beta^{els}_{Faraday}$ and $\beta^{fc}_{Faraday}$) correlation factors estimated by the AOHS in comparison with their theoretical values.
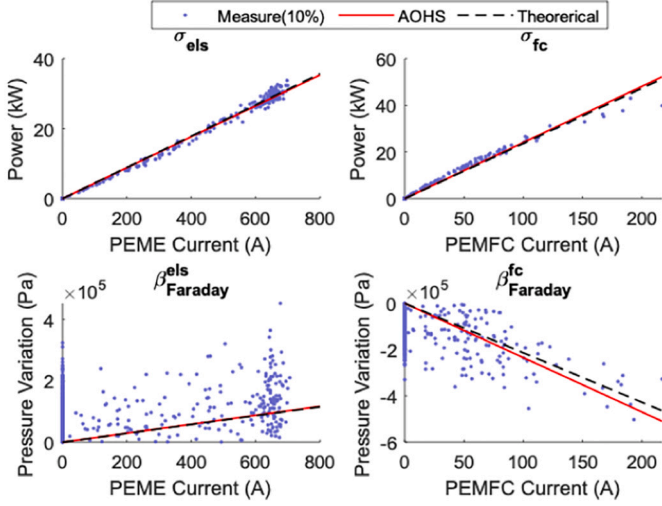
Fig. 10. Comparison between the final estimated model correlation factors (σ_{PEM} and $\beta_{Faraday}^{PEM}$) and their corresponding theoretical values in the case with noise measurement variance of 10 %.

5.2. Comparison with the time-invariant model

The proposed MPC with the AOHS is compared to an MPC with the time-invariant model specified in Eq. (17). This comparison aims to verify the impact of parametric errors on the annual building microgrid self-consumption and coverage rates, as well as the accuracy of day-ahead grid energy planning transmitted to community aggregators.

In this view, the building microgrid and its HMPC (EMPC and TMPC) were simulated in MATLAB Simulink® for 365 days under four scenarios. The first three scenarios are when the HMPC is equipped with a time-invariant hydrogen storage model holding +20 %, 0 %, and −20 % parametric errors in θ_{fc} and θ_{els} defined in Eq. (17). Finally, the fourth scenario is when the HMPC is endowed with the AOHS algorithm with a noise measurement of variance of 5 %. Since no parameter needs to be tuned when employing the AOHS algorithm, it is not necessary to analyse the impact of parametric errors.

$$\tau_{sc} = 1 - \frac{\sum_{k=1}^{8760} E_{grid,k}^{injected}}{\sum_{k=1}^{8760} E_{pv,k}}; \tau_c = 1 - \frac{\sum_{k=1}^{8760} E_{grid,k}^{import}}{\sum_{k=1}^{8760} E_{cons,k}} \quad (34)$$

By comparing the annual self-consumption and annual coverage rates defined by Eq. (34) summarised in Table 4, it is possible to observe that the HMPC with the AOHS algorithm assures practically the same coverage and self-consumption rates as the time-invariant model with no parametric errors. Moreover, by comparing the annual coverage rate of these four simulation scenarios, it is possible to note that it is almost insensitive to parametric errors. In contrast, the self-consumption rate is reduced by 3 p.p. with a parametric error of −20 %, and it was unchanged with a parametric error of +20 %.

The reason behind this result is that the power reference of the PEME is almost the same (around 30 kWh) in the scenarios with the AOHS

Table 4
Comparison of the coverage and self-consumption rates when using time-invariant models and the AOHS algorithm.

	Time-invariant model			AOHS
	−20 %[a]	0 %[a]	+20 %[a]	
Coverage rate (%)	47.1	47.5	47.2	47.4
Self-consumption (%)	94.3	97.1	97.3	97.2

[a] Parametric error included in θ_{fc} and θ_{els}.

algorithm and the time-invariant models with +20 % and 0 %, as shown in Fig. 11. According to Fig. 11, the EMPC minimises the grid energy exchange by using its ESS as much as possible. Consequently, to maximise the self-consumption rate τ_{sc}, the EMPC absorbs the PV energy surplus by storing hydrogen through the operation of the PEME.

As shown in Fig. 11, as in all scenarios the hydrogen tank is not full (the LoH is below 90 %), the EMPC can operate the PEME most of the time at maximum power rate (around 30 kWh) to minimise the grid energy injection. Since there are low parametric errors when employing the AOHS and the time-invariant models with 0 % (Fig. 11b and d), the TMPC can follow the LoH references strictly, resulting in an operation of the PEME close to the maximum power rate, as expected from the EMPC. On the contrary, even though the LoH reference is not followed by the TMPC when θ_{els} is over estimated (Fig. 11c), the power set point of the PEME is equal to the EMPC estimated values. This is because the over-estimation of θ_{els} leads the LoH references to be always higher than the real capacities of the PEME. Therefore, this will induce the PEME to be operated over its estimated capacity, which is bounded by its maximum power rate. Consequently, the power references of both the TMPC and the EMPC are equivalent, assuring similar self-consumption rates.

On the other hand, when θ_{els} is underestimated (Fig. 11a), the errors in the LoH estimation calculated by the EMPC will lead the PEME to be underused. In this scenario, the EMPC tries to operate the PEME at maximum power rate (around 30 kWh), but due to parametric errors in θ_{els} it will transmit to the TMPC the references of the LoH that are smaller than the real hydrogen production rate. Therefore, the PEME will be underexploited, resulting in the reduction of the self-consumption rate.

It is important to note that a similar phenomenon happens with the operation of fuel cells. Nonetheless, due to the low round-trip efficiency (below 40 %) of hydrogen conversion, the use of fuel cells is minimal. According to graphs shown in Fig. 12, even though the annual use of fuel cells can vary up to 17 % (1.3 MWh) regarding the time-invariant model with no errors, this difference is small compared to the annual building consumption, which amounts to 242 MWh/year. Consequently, the coverage rate (τ_c) defined by Eq. (34) is almost unaffected by the inaccuracies in the PEMFC models.

Although the imprecisions in the LoH estimation do not always impact the annual self-consumption and coverage rates, it affects the grid energy planning sent to community aggregators. As shown in Fig. 13, compared to time-invariant models with no parametric errors, the error in the day-ahead grid energy exchange planning sent to the community aggregator increases by respectively 55 % and 10 % with time-invariant (T.I.) models holding −20 % and +20 % of parametric imprecision. Conversely, the proposed AOHS algorithm can assure an average error of 334 Wh, which is 52 % lower than the ideal time-invariant. This result indicates that the AOHS algorithm can facilitate grid energy management from the point of view of the external grid by providing more reliable day-ahead grid energy planning to community aggregators.

6. Conclusion

In this paper, a two-level hierarchical model predictive controller (HMPC) with an Autonomous Observer of Hydrogen Storage was proposed to reduce the HMPC internal model inaccuracy. This modelling inaccuracy issue is particularly important when considering long operating times. The proposed solution incorporates an external observer to the HMPC structure, requiring little to no modification of the MPC algorithms while offering better performance. Even subjected to strong measurement noise, the designed energy management proved capable of identifying the real hydrogen production and consumption rates. This operation was performed while relying only on a few storage variables and requiring no tuning of the parameters. This facilitates its implementation in embedded systems. It could guarantee an average precision inferior to 2 % points regarding the theoretical model that holds the full knowledge of the system.
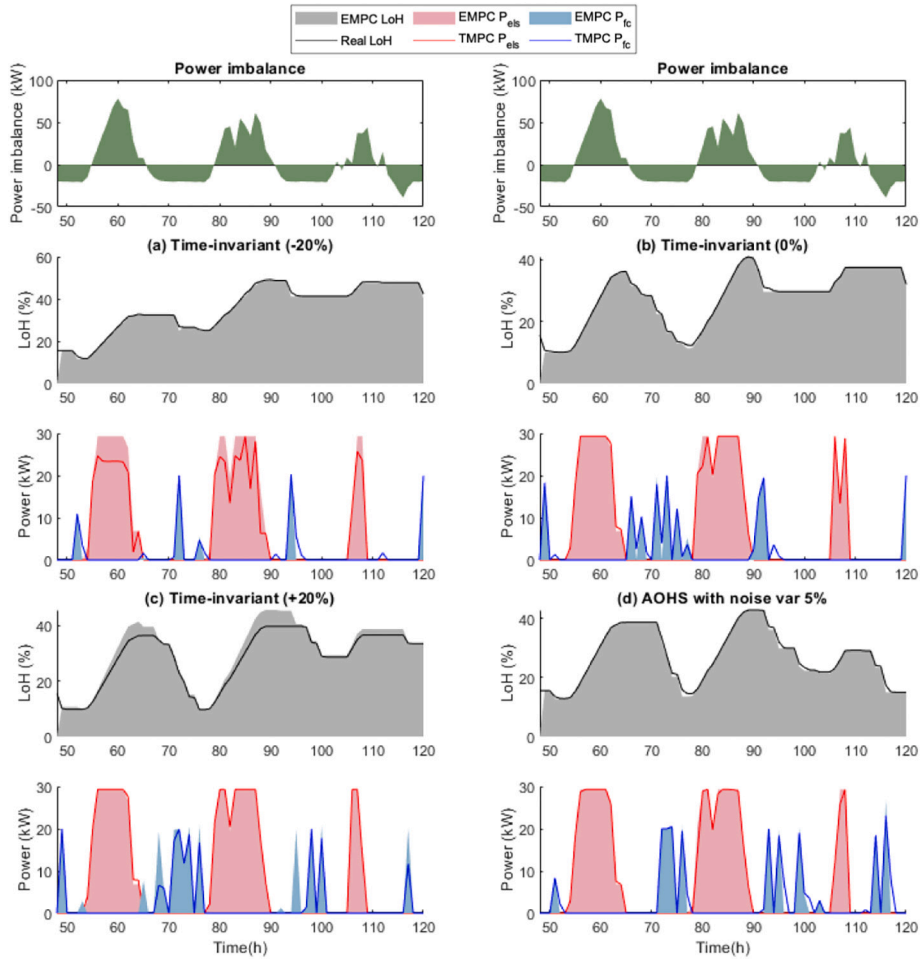
Fig. 11. Comparison between the EMPC and TMPC control variables with the AOHS algorithm subjected to measurement noise of 5 % and with time-invariant models subjected to parametric errors of −20 %, 0 %, and +20 %.
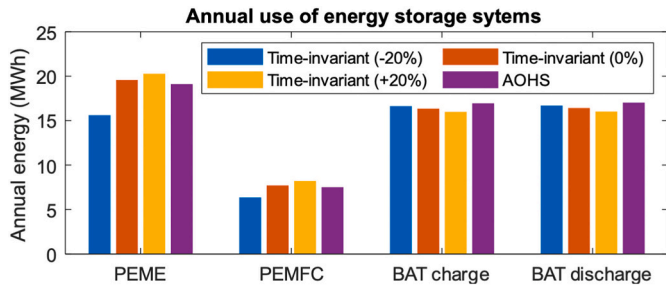

Fig. 12. Annual use of energy storage systems when using time-invariant models with parametric errors and the AOHS algorithm with noise measurement of 5 %.

Fig. 13. Average (red squares) and standard deviation (blue bars) of the error in the day-ahead grid energy exchange planning sent to community aggregator. (For interpretation of the references to color in this figure legend, the reader is referred to the web version of this article.)

The flexibility of the algorithm in adapting automatically to external environments reduces the negative effects of model parameter inaccuracies provided by manufacturers. Through simulations, it was noticed that a 20 % underestimation of hydrogen production reduces the building's annual self-consumption by about 3 % when using a rudimentary model approach. On the other hand, through a more accurate estimation of the tank level hydrogen provided by the novel algorithm, the self-consumption and coverage rates are similar to the ideal model that holds the full system knowledge. Additionally, the algorithm enables the HMPC to provide reliable day-ahead grid energy planning to community aggregators, facilitating the external grid energy management and reducing the errors by about 52 % compared with the conventional modelling approach.
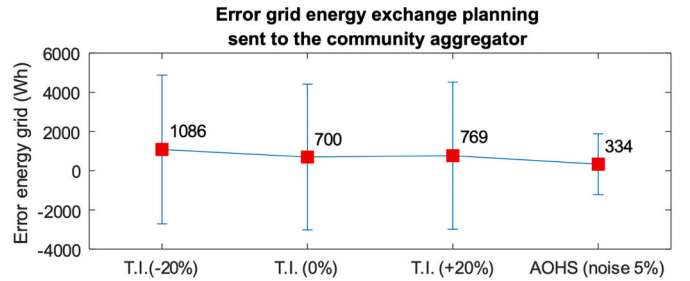
Since the ESTIA's building microgrid studied in this paper is under construction, the future work consists of testing the algorithms and solutions described in this paper using hardware in the loop approach. The fact that the three elements of the control structure described in this paper, EMPC, TMPC and AOHS, are operating with different time scales will make possible to implement them using different machines or different cores of the same real-time computer for each control element.

CRediT authorship contribution statement

- Daniela Yassuda Yamahita

  Conceptualization; Methodology; Software; Validation; Formal analysis; Investigation; Data Curation; Writing - Original draft; Writing - Review & editing; Visualization; Project administration
- Ionel Vechiu

  Conceptualization; Validation; Resources; Writing - Review & editing; Supervision; Project administration; Funding acquisition
- • Jean-Paul Gaubert

  Conceptualization; Validation; Resources; Writing - Review & editing; Supervision; Project administration; Funding acquisition
- • Samuel Jupin

  Paper revision and discussion over the review comments.

Declaration of competing interest

The authors declare the following financial interests/personal relationships which may be considered as potential competing interests: Daniela Yassuda Yamashita reports financial support was provided by Region Nouvelle-Aquitaine. Jean-Paul Gaubert reports a relationship with University of Poitiers that includes: employment. Ionel Vechiu reports a relationship with ESTIA-RECHERCHE that includes: employment. Daniela Yassda Yamashita reports a relationship with ESTIA-RECHERCHE that includes: employment.

References

[1] Perspective for the Clean Energy Transition 2019 - The Critical Role of Buildings, International Energy Agency, Apr. 2019.

[2] M. Hu, F. Xiao, S. Wang, Neighborhood-level coordination and negotiation techniques for managing demand-side flexibility in residential microgrids, Renew. Sustain. Energy Rev. 135 (Jan. 2021), 110248, https://doi.org/10.1016/j.rser.2020.110248.

[3] Y. Wu, Y. Wu, H. Cimen, J.C. Vasquez, J.M. Guerrero, Towards collective energy community: potential roles of microgrid and blockchain to go beyond P2P energy trading, Appl. Energy 314 (May 2022), 119003, https://doi.org/10.1016/j.apenergy.2022.119003.

[4] H. Fontenot, B. Dong, Modeling and control of building-integrated microgrids for optimal energy management – a review, Appl. Energy 254 (Nov. 2019), 113689, https://doi.org/10.1016/j.apenergy.2019.113689.

[5] G.K. Farinis, F.D. Kanellos, Integrated energy management system for microgrids of building prosumers, Electr. Power Syst. Res. 198 (Sep. 2021), 107357, https://doi.org/10.1016/j.epsr.2021.107357.

[6] G. Masson, F. Tilli, L. Calleri, Solar PV self-consumption, in: Comprehensive Renewable Energy, Elsevier, 2022, pp. 144–159, https://doi.org/10.1016/B978-0-12-819727-1.00141-2.

[7] T. Gomez, et al., European Union electricity markets: current practice and future view, IEEE PowerEnergy Mag. 17 (1) (Jan. 2019) 20–31, https://doi.org/10.1109/MPE.2018.2871739.

[8] E.A. Bartels, T. Pippia, B. De Schutter, Influence of hydrogen on grid investments for smart microgrids, Int. J. Electr. Power Energy Syst. 141 (Oct. 2022), 107968, https://doi.org/10.1016/j.ijepes.2022.107968.

[9] H. Ren, Q. Wu, W. Gao, W. Zhou, Optimal operation of a grid-connected hybrid PV/fuel cell/battery energy system for residential applications, Energy 113 (Oct. 2016) 702–712, https://doi.org/10.1016/j.energy.2016.07.091.

[10] J. Lokar, P. Virtič, The potential for integration of hydrogen for complete energy self-sufficiency in residential buildings with photovoltaic and battery storage systems, Int. J. Hydrogen Energy (May 2020), https://doi.org/10.1016/j.ijhydene.2020.04.170 p. S0360319920315743.

[11] V.M. Maestre, A. Ortiz, I. Ortiz, Challenges and prospects of renewable hydrogen-based strategies for full decarbonization of stationary power applications, Renew. Sustain. Energy Rev. 152 (Dec. 2021), 111628, https://doi.org/10.1016/j.rser.2021.111628.

[12] M.C. Argyrou, P. Christodoulides, S.A. Kalogirou, Energy storage for electricity generation and related processes: technologies appraisal and grid scale applications, Renew. Sustain. Energy Rev. 94 (Oct. 2018) 804–821, https://doi.org/10.1016/j.rser.2018.06.044.

[13] D.Y. Yamashita, I. Vechiu, J.-P. Gaubert, A review of hierarchical control for building microgrids, Renew. Sustain. Energy Rev. 118 (Feb. 2020), 109523, https://doi.org/10.1016/j.rser.2019.109523.

[14] M.F. Zia, E. Elbouchikhi, M. Benbouzid, Microgrids energy management systems: a critical review on methods, solutions, and prospects, Appl. Energy 222 (Jul. 2018) 1033–1055, https://doi.org/10.1016/j.apenergy.2018.04.103.

[15] L. Valverde, C. Bordons, F. Rosa, Integration of fuel cell technologies in renewable-energy-based microgrids optimizing operational costs and durability, IEEE Trans. Ind. Electron. 63 (1) (Jan. 2016) 167–177, https://doi.org/10.1109/TIE.2015.2465355.

[16] J. Hu, Y. Shan, J.M. Guerrero, A. Ioinovici, K.W. Chan, J. Rodriguez, Model predictive control of microgrids – an overview, Renew. Sustain. Energy Rev. 136 (Feb. 2021), 110422, https://doi.org/10.1016/j.rser.2020.110422.

[17] F. Kamal, B. Chowdhury, Model predictive control and optimization of networked microgrids, Int. J. Electr. Power Energy Syst. 138 (Jun. 2022), 107804, https://doi.org/10.1016/j.ijepes.2021.107804.

[18] F. Garcia-Torres, C. Bordons, Optimal economical schedule of hydrogen-based microgrids with hybrid storage using model predictive control, IEEE Trans. Ind. Electron. 62 (8) (Aug. 2015) 5195–5207, https://doi.org/10.1109/TIE.2015.2412524.

[19] R. García-Valverde, N. Espinosa, A. Urbina, Simple PEM water electrolyser model and experimental validation, Int. J. Hydrog. Energy 37 (2) (Jan. 2012) 1927–1938, https://doi.org/10.1016/j.ijhydene.2011.09.027.

[20] Z. Abdin, C.J. Webb, E.MacA. Gray, PEM fuel cell model and simulation in Matlab–Simulink based on physical parameters, Energy 116 (Dec. 2016) 1131–1144, https://doi.org/10.1016/j.energy.2016.10.033.

[21] H. Yuan, H. Dai, X. Wei, P. Ming, Model-based observers for internal states estimation and control of proton exchange membrane fuel cell system: a review, J. Power Sources 468 (Aug. 2020), 228376, https://doi.org/10.1016/j.jpowsour.2020.228376.

[22] B. Bendib, H. Belmili, F. Krim, A survey of the most used MPPT methods: conventional and advanced algorithms applied for photovoltaic systems, Renew. Sustain. Energy Rev. 45 (May 2015) 637–648, https://doi.org/10.1016/j.rser.2015.02.009.

[23] JRC Photovoltaic Geographical Information System (PVGIS) - European Commission. https://re.jrc.ec.europa.eu/pvg_tools/en/tools.html#MR. (Accessed 5 March 2020).

[24] F. Moret, P. Pinson, Energy collectives: a community and fairness based approach to future electricity markets, IEEE Trans. Power Syst. 34 (5) (Sep. 2019) 3994–4004, https://doi.org/10.1109/TPWRS.2018.2808961.

[25] Commission de Régulation de l'Energie, Cahier des charges de l'appel d'offres portant sur la réalisation et l'exploitation d'Installations de production d'électricité à partir d'énergies renouvelables en autoconsommation et situées en métropole continentale, Dec. 26, 2019.

[26] C. Rakousky, et al., Polymer electrolyte membrane water electrolysis: restraining degradation in the presence of fluctuating power, J. Power Sources 342 (Feb. 2017) 38–47, https://doi.org/10.1016/j.jpowsour.2016.11.118.

[27] Z. Abdin, C.J. Webb, E.MacA. Gray, Modelling and simulation of a proton exchange membrane (PEM) electrolyser cell, Int.J.Hydrogen Energy 40 (39) (Oct. 2015) 13243–13257, https://doi.org/10.1016/j.ijhydene.2015.07.129.

[28] C. Wang, in: Modelling and control of hybrid wind/photovoltaic/fuel cell distributed generation systems, 2006, p. 402.

[29] Enedis l'électricité en réseau, Conditions de raccordement des Installations de stockage, Oct. 2017.

[30] D.Yassuda Yamashita, I. Vechiu, J.-P. Gaubert, "Real-time Parameters Identification of Lithium-ion Batteries Model to Improve the Hierarchical Model Predictive Control of Building MicroGrids," presented at the 2020 22nd European Conference on Power Electronics and Applications (EPE '20 ECCE Europe), Lyon, Sep. 2020, https://doi.org/10.23919/EPE20ECCEEurope43536.2020.9215878.

[31] D.Yassuda Yamashita, I. Vechiu, J.-P. Gaubert, Two-level hierarchical model predictive control with an optimised cost function for energy management in building microgrids, Appl. Energy 285 (Mar. 2021) 116420, https://doi.org/10.1016/j.apenergy.2020.116420.

[32] S.M. Njoya, O. Tremblay, L.-A. Dessaint, A generic fuel cell model for the simulation of fuel cell vehicles, in: 2009 IEEE Vehicle Power And Propulsion Conference, Dearborn, MI, Sep. 2009, pp. 1722–1729, https://doi.org/10.1109/VPPC.2009.5289692.